

This work was written as part of one of the author's official duties as an Employee of the United States Government and is therefore a work of the United States Government. In accordance with 17 U.S.C. 105, no copyright protection is available for such works under U.S. Law.

Public Domain Mark 1.0

<https://creativecommons.org/publicdomain/mark/1.0/>

Access to this work was provided by the University of Maryland, Baltimore County (UMBC) ScholarWorks@UMBC digital repository on the Maryland Shared Open Access (MD-SOAR) platform.

**Please provide feedback**

Please support the ScholarWorks@UMBC repository by emailing [scholarworks-group@umbc.edu](mailto:scholarworks-group@umbc.edu) and telling us what having access to this work means to you and why it's important to you. Thank you.



# Radial Variations in Solar Type III Radio Bursts

Vratislav Krupar<sup>1,2</sup> , Oksana Kruparova<sup>1,2</sup> , Adam Szabo<sup>2</sup> , Lynn B. Wilson, III<sup>2</sup> , Frantisek Nemec<sup>3</sup> ,  
 Ondrej Santolik<sup>3,4</sup> , Marc Pulupa<sup>5</sup> , Karine Issautier<sup>6</sup> , Stuart D. Bale<sup>5,7</sup> , and Milan Maksimovic<sup>6</sup>

<sup>1</sup> Goddard Planetary Heliophysics Institute, University of Maryland, Baltimore County, Baltimore, MD 21250, USA; [vratislav.krupar@nasa.gov](mailto:vratislav.krupar@nasa.gov)  
<sup>2</sup> Heliospheric Physics Laboratory, Heliophysics Division, NASA Goddard Space Flight Center, Greenbelt, MD 20771, USA  
<sup>3</sup> Faculty of Mathematics and Physics, Charles University, 121 16 Prague, Czech Republic  
<sup>4</sup> Department of Space Physics, Institute of Atmospheric Physics of the Czech Academy of Sciences, 141 00 Prague, Czech Republic  
<sup>5</sup> Space Sciences Laboratory, University of California, Berkeley, CA 94720, USA  
<sup>6</sup> LESIA, Observatoire de Paris, Université PSL, CNRS, Sorbonne Université, Université de Paris, F-92195 Meudon, France  
<sup>7</sup> Physics Department, University of California Berkeley, Berkeley, CA 94720, USA

Received 2024 January 25; revised 2024 May 14; accepted 2024 May 14; published 2024 May 28

## Abstract

Type III radio bursts are generated by electron beams accelerated at reconnection sites in the corona. This study, utilizing data from the Parker Solar Probe's first 17 encounters, closely examines these bursts down to 13 solar radii. A focal point of our analysis is the near-radial alignment (within  $5^\circ$ ) of the Parker Solar Probe, STEREO-A, and Wind spacecraft relative to the Sun. This alignment, facilitating simultaneous observations of 52 and 27 bursts by STEREO-A and Wind respectively, allows for a detailed differentiation of radial and longitudinal burst variations. Our observations reveal no significant radial variations in electron beam speeds, radio fluxes, or exponential decay times for events below 50 solar radii. In contrast, closer to the Sun we noted a decrease in beam speeds and radio fluxes. This suggests potential effects of radio beaming or alterations in radio source sizes in this region. Importantly, our results underscore the necessity of considering spacecraft distance in multispacecraft observations for accurate radio burst analysis. A critical threshold of 50 solar radii emerges, beyond which beaming effects and changes in beam speeds and radio fluxes become significant. Furthermore, the consistent decay times across varying radial distances point toward a stable trend extending from 13 solar radii into the inner heliosphere. Our statistical results provide valuable insights into the propagation mechanisms of type III radio bursts, particularly highlighting the role of scattering near the radio source when the frequency aligns with the local electron plasma frequency.

*Unified Astronomy Thesaurus concepts:* [Radio astronomy \(1338\)](#); [Radio bursts \(1339\)](#)

## 1. Introduction

Type III radio bursts, marked by their rapid frequency drifts, are a dynamic manifestation of solar activity, observable across a wide range of frequencies. These bursts are produced by suprathermal electron beams, accelerated at reconnection sites in the corona and traveling outward along open magnetic field lines through the corona and interplanetary medium (Wild 1950; Dulk 2000; Reid & Ratcliffe 2014). As these beams traverse, they interact with the ambient medium, generating radio emissions predominantly at the electron plasma frequency ( $f_{pe}$ ) for the fundamental component and its first harmonic ( $2f_{pe}$ ), through the plasma emission mechanism (Ginzburg & Zhelezniakov 1958; Cairns & Robinson 1995). Both components, commonly observed at decametric and shorter wavelengths, become indistinct at longer wavelengths, particularly in interplanetary space, posing challenges in their differentiation (Dulk & Suzuki 1980; Kellogg 1980; Reiner et al. 1998; Gopalswamy et al. 2005).

Type III radio bursts are detectable across a broad range of angles, even from sources situated behind the Sun. Intriguingly, their apparent source regions often extend to larger radial distances than initially anticipated, at times appearing to envelop a substantial portion of the inner heliosphere (Bonnin et al. 2008; Krupar et al. 2014). This widespread and diffuse

manifestation is primarily attributed to the scattering of radio waves by electron density inhomogeneities as they travel from the source to the spacecraft (Steinberg et al. 1984; Bastian 1994; Kontar et al. 2017, 2019, 2023; Krupar et al. 2024a). Such scattering effects can create an illusion of larger source regions, making it appear as though the bursts fill a considerable part of the inner heliosphere. This phenomenon leads to the spacecraft antennas being immersed in signals from multiple directions. These bursts can last from minutes to hours, frequently exhibiting an exponential decay in radio flux density (Krupar et al. 2018), adding complexity to their analysis.

The advent of multispacecraft missions has ushered in a new era for studying solar radio bursts. The concurrent observations from diverse vantage points, as provided by missions like Parker Solar Probe, Solar Orbiter, STEREO-A, and Wind, enhance the precision and reliability of radio burst tracking (Musset et al. 2021; Badman et al. 2022; Chen et al. 2023). Recently, Krupar et al. (2024b) introduced two novel localization techniques for analyzing four-spacecraft observations. The first method employs intensity fitting using a circular Gaussian distribution to analyze relative radio fluxes observed by the spatially separated spacecraft. This approach assumes that the radio flux diminishes following a  $1/r^2$  pattern. The second method focuses on the timing of radio burst arrivals, employing a similar circular Gaussian distribution for analysis. This development not only enables accurate tracking of radio bursts but also facilitates a deeper understanding of their associations with solar flares, potentially advancing our knowledge of solar flare dynamics through radio observations.



Original content from this work may be used under the terms of the [Creative Commons Attribution 4.0 licence](#). Any further distribution of this work must maintain attribution to the author(s) and the title of the work, journal citation and DOI.

In this Letter, we conduct a statistical survey of type III radio bursts as observed by two spacecraft nearly aligned radially. Section 2 is dedicated to an extensive case study of three events and statistical examination, utilizing data acquired from the Parker Solar Probe, along with the STEREO-A/WAVES and Wind/WAVES instruments. This section methodically presents the data analysis, elucidating the nuanced characteristics of these bursts. Section 3 delves into the interpretation of our results. Here, we integrate and discuss the implications of our findings, particularly focusing on the propagation mechanisms of type III bursts and the influence of scattering phenomena in proximity to the radio source.

## 2. Observations and Analysis

We present an in-depth analysis of data recorded by the Parker Solar Probe during its first 17 encounters, reaching as close as 11 solar radii ( $1 R_{\odot} = 695,500$  km) from the Sun (Fox et al. 2016). A key aspect of our study is the identification of periods when the spacecraft was radially aligned within  $5^{\circ}$  with STEREO-A or the Wind spacecraft located near 1 au ( $1 \text{ au} = 149,598,000$  km). This specific alignment enables us to distinguish between radial and longitudinal variations in type III radio bursts.

Our primary data source is the Radio Frequency Spectrometer (RFS; Pulupa et al. 2017), part of the FIELDS suite (Bale et al. 2016) aboard the Parker Solar Probe. The RFS, functioning as a two-channel digital receiver and spectrometer, provided electric field measurements in the range of 10.5 kHz to 19.2 MHz. We utilized data from the RFS's Low Frequency Receiver, which is equipped with 64 logarithmically spaced frequency channels between 10.5 kHz and 1.7 MHz, offering a temporal resolution of 7 s.

For STEREO-A (Kaiser et al. 2008), data were sourced from the High Frequency Receiver (HFR), a component of the STEREO/WAVES instrument suite (Bougeret et al. 2008). The HFR, a dual-channel receiver with a frequency range of 125 kHz to 16 MHz and a temporal resolution of 35 s, is vital for determining the direction of arrival, flux, and polarization properties of electromagnetic waves (Cecconi et al. 2008; Krupar et al. 2022).

Regarding the Wind spacecraft (Wilson et al. 2021), we analyze measurements from its WAVES instrument, specifically using the Radio Receiver Band 1 (RAD1) and Radio Receiver Band 2 (RAD2) radio receivers, which capture electric field data between 20 kHz and 13.8 MHz. Our focus is on RAD1 data, offering direction-finding capabilities in the 20 kHz to 1040 kHz range, with a 3 kHz effective bandwidth and a temporal resolution of 45 s (Bougeret et al. 1995). To analyze direction-finding data from Wind/WAVES, we employed specialized techniques designed for spinning spacecraft (Manning & Fainberg 1980; Hoang et al. 1981) updated by Bonnin et al. (2023).

Our analysis encompasses a rigorous statistical examination of 52 type III radio bursts observed by the Parker Solar Probe and STEREO-A from August 2021 to September 2023. Additionally, we analyzed 27 type III radio bursts detected concurrently by the Parker Solar Probe and Wind between June and September 2023. During this interval, the Parker Solar Probe approached the Sun to within  $11 R_{\odot}$ . The Appendix provides detailed insights into the event identification process.

In this study, our selection of intense, simple, and isolated type III radio bursts for analysis was conducted with precision,

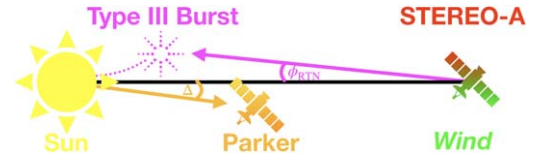


**Figure 1.** Illustrative Sketch of the Sun, radio burst, and spacecraft positions. This diagram presents the Sun, with the spatial relationship and alignment of the radio burst and the spacecraft (Parker Solar Probe, STEREO-A, or Wind). The angle symbolized by  $\Delta$  represents the angle between the Sun-STEREO-A (or Sun-Wind) line and the location of the Parker Solar Probe. The angle  $\phi_{\text{RTN}}$ , on the other hand, indicates the deviation of the radio burst's wavevector from the Sun-STEREO-A (or Sun-Wind) line.

particularly when the Parker Solar Probe was in radial alignment with either STEREO-A or Wind. To ensure the accuracy and reliability of our observations, we employed a stringent criterion for radial alignment, restricting the spacecraft's location to within  $5^{\circ}$  of alignment. This specific angle, denoted as  $\Delta$ , was chosen to be below  $5^{\circ}$  (Figure 1), a decision grounded in a thorough evaluation of the uncertainties inherent in direction-finding techniques.

The rationale behind adopting a  $5^{\circ}$  threshold is meticulously justified by the direction-finding uncertainty analysis presented in Krupar et al. (2012), where Figure 7 illustrates this margin as a conservative estimate of such uncertainties. This approach, therefore, is not arbitrary but is designed to robustly accommodate potential variances in measurement that could affect the integrity of our analysis. By adhering to this conservative threshold, we aim to strike a careful balance between achieving specificity in our event selection and acknowledging the practical limitations posed by the current capabilities of observational technologies.

### 2.1. Case Study Analysis: Electron Beam Speeds

Figure 2 presents a case study of three type III radio bursts from our data set, captured during encounters 12 and 15. This analysis highlights a notable burst observed on 2023 March 18, when the spacecraft was at  $13.5 R_{\odot}$  (Case #1), and two additional events from 2022 June 3, with the probe located at  $20.2 R_{\odot}$  and  $21.9 R_{\odot}$ , respectively (Case #2 and Case #3). These moments, particularly Case #1, represent the most extensive separation distances in our data set, providing an excellent opportunity to study type III burst characteristics at varying solar proximities. These three cases are the closest events to the Sun in our statistical database and form the basis of our further discussion in this Letter. Figure 2(m) illustrates the relative nonradial distances of the Parker Solar Probe with respect to STEREO-A as a function of radial distance from the Sun, represented in orange for all three cases. In all cases, the nonradial deviation from the Sun-STEREO-A line was approximately  $1 R_{\odot}$ , indicating a nearly radial alignment with STEREO-A.

Case #1 was contemporaneous with a C3.8 solar flare, initiating at 00:27, peaking at 00:37, and concluding at 00:42 UTC on 2023 March 18. This flare originated from NOAA active region (AR) 13256, located at S24E79. Case #2 correlated with a B8.1 solar flare that began at 02:27, reached its peak at 02:48, and ended at 02:52 UTC on 2022 June 3, emanating from NOAA AR 13024 at S33W34. Case #3 corresponded to a B6.7 solar flare, starting at 07:11, peaking at 07:20, and ceasing at 07:25 UTC on the same day, 2022 June 3, from NOAA AR 13024, also at S33W35.



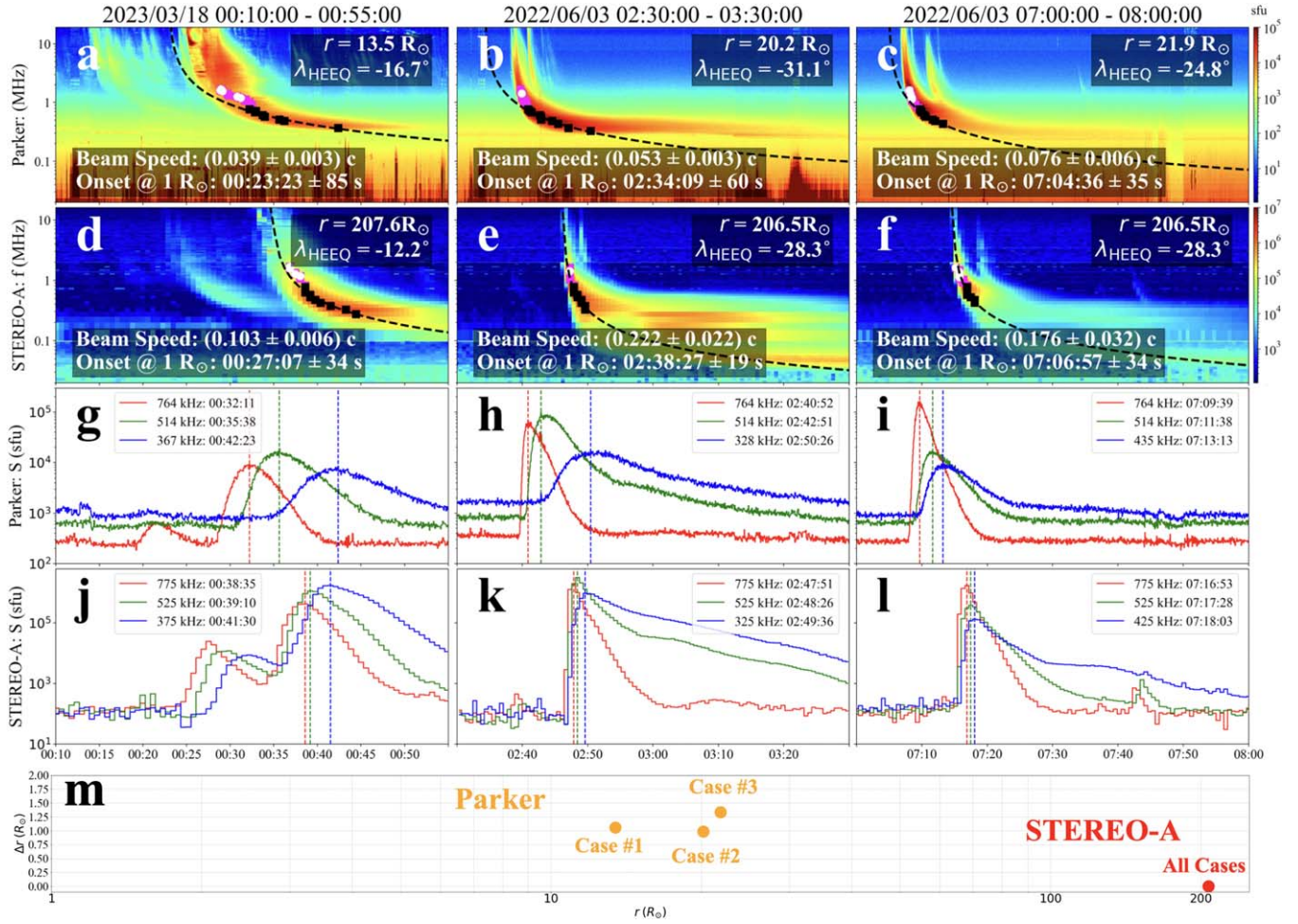


**Figure 2.** Radio measurements from the Parker Solar Probe (panels (a)–(c) and (g)–(i)) and STEREO-A (panels (d)–(f) and (j)–(l)) on 2023 March 18 between 00:10 and 00:55 UT (Case #1, left column), on 2022 June 3 between 02:30 and 03:30 UT (Case #2, middle column), and on 2022 June 3 between 07:00 and 08:00 UT (Case #3, right column). Panels (a)–(g) mark peak fluxes within our targeted frequency range using squares. Black squares denote peak fluxes used to calculate electron beam speeds based on the empirical density model, with fitted electron beams shown by black dashed lines and the computed speeds and onset times at  $1 R_{\odot}$  noted in each panel. Magenta squares highlight peak fluxes outside our propagation analysis frequency range. White circles indicate peak fluxes when the wavevector azimuth ( $\phi_{\text{RTN}}$ ) was within  $5^{\circ}$ , implying minimal radio propagation variation and suggesting that the type III bursts originated near the line connecting the Parker Solar Probe, STEREO-A, and the Sun. Panels (g)–(l) display fixed-frequency light curves for three frequency channels, utilized in calculating apparent beam speeds, with peak times marked by vertical dashed lines. Panel (m) illustrates the relative nonradial distances of the Parker Solar Probe with respect to STEREO-A as a function of radial distance from the Sun, represented in orange for all three cases. The position of STEREO-A is denoted in red.

In terms of spatial alignment, the solar flare for Case #1 was situated approximately  $63^{\circ}$  eastward relative to the Parker Solar Probe–Sun line. For Cases #2 and #3, the solar flares were located  $62^{\circ}$  and  $60^{\circ}$  westward, respectively. While an ideal observational scenario would feature solar flares occurring within  $5^{\circ}$  of the Sun–spacecraft line, especially during significant spacecraft separations, such perfectly aligned events were not present within our data set. This reality underscores the observational challenges inherent in studying these dynamic solar events.

In all cases studied by the Parker Solar Probe, a distinct low-frequency cutoff emerged around 200 kHz, corresponding to the local plasma frequency,  $f_{\text{pe}}$ . This heightened plasma frequency observed by the Parker Solar Probe, as opposed to STEREO, is attributable to the increased plasma density closer to the Sun. As a result, our analysis specifically targeted radio emissions above 275 kHz for both the Parker Solar Probe and STEREO-A. We set the upper frequency limit at 1.7 MHz, which corresponds to the maximum capability of the RFS/LFR instrument. This chosen frequency range is compatible with the

direction-finding data from STEREO-A, which spans 125 kHz to 2 MHz. Our detailed analysis involved a close examination of peak fluxes within the 275 kHz to 1.7 MHz frequency range. These specific frequencies are marked as squares in Figure 2. Across the cases studied, no Langmuir waves were detected. We examined the polarization characteristics of the observed type III bursts to determine if they could be used to differentiate between fundamental and harmonic components. However, none of the bursts exhibited significant circular polarization. This lack of significant circular polarization indicates that polarization measurements are not effective for distinguishing between fundamental and harmonic emissions in our data. Consequently, there remains an uncertainty as to whether the observed emissions are fundamental or harmonic components.

In our investigation, we analyzed the radial evolution of spectral features in type III radio bursts, leveraging observations from the Parker Solar Probe and STEREO-A. A key aspect of our analysis focused on determining beam speeds using a density model of Kruparova et al. (2023). For instance, in Case #1, we identified pronounced spectral features, notably

fine structures, above 1 MHz as captured by the Parker Solar Probe (refer to Figure 2(a)), which were not as distinctly observed by STEREO-A (refer to Figure 2(d)). These features bear resemblance to the characteristics of type IIIb–type III pair bursts, suggesting complex interactions within the emission source regions (Sharykin et al. 2018). Such a comparison raises the possibility that what we observe at the Parker Solar Probe could be indicative of either the fundamental or the harmonic components of radio emission, components that might not be as discernible when observed by STEREO-A at 1 au.

Moreover, in Case #2, we noted a different kind of complexity with structures observed below 200 kHz by STEREO-A (Figure 2(e)) though these observations were beyond our primary frequency focus of 275 kHz to 1.7 MHz. The distinction in observed spectral features across these cases underscores the variability in radio burst emissions and highlights the potential for fundamental or harmonic interpretations depending on the observing spacecraft’s relative position and the employed frequency range.

Our analysis also included examining the frequency drift of the lower-frequency portion (275 to 775 kHz, in 50 kHz steps, marked by black squares in Figure 2) of the type III bursts. Drawing on a power-law model for electron density as a function of radial distance by Kruparova et al. (2023)—a model based on electron density measurements in the solar wind from the Parker Solar Probe’s first 15 encounters—we approached the bursts as fundamental emissions with exciter beams moving at constant radial speeds. This allowed us to calculate beam velocities from the observed frequency drifts using the aforementioned density model. By tracing the electron beams back to their solar surface origins, we could estimate separate onset times for the bursts at both spacecraft.

Our analysis intriguingly showed that the beam speeds observed at STEREO-A were consistently higher than those measured by the Parker Solar Probe for all three studied events. This pattern suggests that the frequency drift of type III radio bursts is faster when observed at 1 au compared to closer proximities to the Sun. Specifically, the electron beam speed ratios calculated for these events were 0.379, 0.239, and 0.432, respectively.

Additionally, we sought to validate the robustness of our observations by employing the density model proposed by Leblanc et al. (1998). This model, which generally predicts lower electron beam speeds—for instance, in Case #1, the speeds are calculated to be 0.029 c and 0.077 c, in contrast to the 0.039 c and 0.103 c derived using our primary model—nonetheless resulted in speed ratios of 0.377, 0.241, and 0.427. These ratios are remarkably consistent with those obtained from our initial analysis.

This agreement between the results yielded by the Leblanc et al. (1998) model and our primary density model underscores the reliability of our findings. It indicates that the conclusions drawn from our study are robust and not overly reliant on the choice of a specific electron density model. Such consistency across different models serves to strengthen the validity of our observations, reinforcing the notion that the behaviors we have documented are intrinsic to the type III radio bursts themselves, rather than artifacts of model selection. Additionally, we observed a discrepancy between the model fit at higher frequencies and the radio data from the Parker Solar Probe, while the fit was notably more accurate for STEREO-A across the entire range of the radio bursts.

In Figures 2(g)–(l), we present fixed-frequency light curves for three frequency channels, highlighting the times of peak fluxes with color-coded dashed lines. These visual representations underscore the significant difference in frequency drift rates between the two spacecraft. The faster drift rate at STEREO-A is evident, contrasting with the comparatively slower drift observed at the Parker Solar Probe. This difference in drift rates provides valuable insights into the spatial variations in the properties of type III radio bursts as they propagate through the heliosphere.

## 2.2. Case Study Analysis: Radio Wave Propagation

Next, we focused on direction-finding data from STEREO-A to study radio wave propagation. This involved incorporating wavevector azimuth ( $\phi_{\text{RTN}}$ ) data in the radial–tangential–normal (RTN) coordinate system. As depicted in Figures 3(a)–(c), we examined  $\phi_{\text{RTN}}$  as a function of frequency for peak fluxes. Data points within  $5^\circ$  of the Sun’s direction are marked as squares. We found that absolute azimuths below 1 MHz were significantly greater than  $5^\circ$  in Case #1, while moderately exceeding this value in Cases #2 and #3. Our selection criterion of restricting absolute azimuths below  $5^\circ$  yielded 11 data points for statistical analysis: 5 from Case #1, 1 from Case #2, and 5 from Case #3.

Figures 3(d)–(f) compare radio flux measurements ( $S$ ) from STEREO-A (in red) and Parker Solar Probe (in orange). We normalized these fluxes to a 1 au distance using a  $1/r^2$  profile, where the radio flux density, measured in solar flux units, is standardized as

$$S = S_{\text{W}} \times 10^{22} \times r_{\text{au}}^2, \quad (1)$$

with  $S_{\text{W}}$  representing the radio flux in watt per meter squared per Hertz and  $r_{\text{au}}$  denoting the spacecraft distance from the Sun in astronomical units (Tapping 2013). We observed varying trends in radio flux measurements across the three cases. Specifically, for Case #1, where the Parker Solar Probe was at  $13 R_{\odot}$ , the radio flux was an order of magnitude lower compared to that measured by STEREO-A. In contrast, for Cases #2 and #3, where the probe was at  $20 R_{\odot}$  and  $22 R_{\odot}$  respectively, the difference in radio flux was about half that of Case #1. Our observations challenge the adequacy of the inverse-square law ( $1/r^2$ ) for radio signal propagation at distances below  $50 R_{\odot}$  from the Sun, suggesting that solar proximity significantly alters both the propagation and intensity of radio emissions. This necessitates the consideration of more complex models to accurately describe radio emission behaviors in these near-Sun environments.

Figures 3(g)–(i) present the exponential decay times ( $\tau$ ) as a function of frequency ( $f$ ) for peak fluxes. Our analysis is based on the premise that the flux density ( $S$ ) diminishes following an exponential decay profile, which is mathematically represented as

$$S(t) = \frac{I}{\tau} \exp\left(-\frac{t_{\text{peak}} - t}{\tau}\right). \quad (2)$$

In this equation,  $t$  denotes the time, while  $t_{\text{peak}}$  is the time at which peak flux density occurs. The coefficients  $I$  (peak radio flux) and  $\tau$  (decay time) are key parameters derived using a gradient-expansion algorithm to compute a nonlinear least-squares fit (Krupar et al. 2018). This approach allows for an



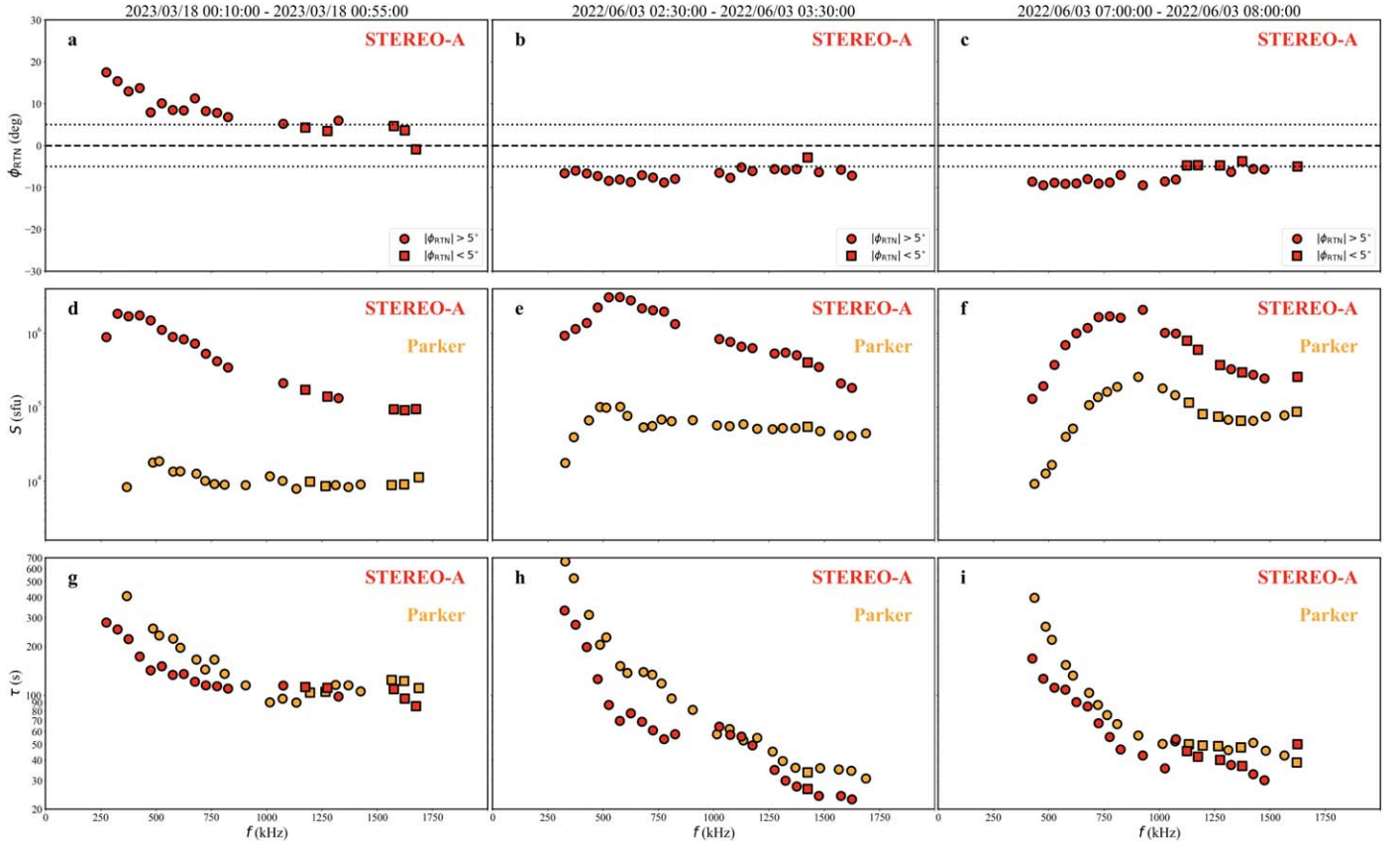


**Figure 3.** Detailed analysis of radio measurements on 2023 March 18 between 00:10 and 00:55 UT (left column), on 2022 June 3 between 02:30 and 03:30 UT (middle column), and on 2022 June 3 between 07:00 and 08:00 UT (right column). Panels (a)–(c) illustrate the wavevector azimuth ( $\phi_{\text{RTN}}$ ) for peak fluxes across various frequencies, as observed by STEREO-A, depicted in red. These panels include dotted black lines marking the  $5^\circ$  boundary for a reference. Panels (d)–(f) display the radio flux measurements, contrasting STEREO-A’s data (in red) with Parker Solar Probe’s observations (in orange). Panels (g)–(i) focus on the exponential decay times  $\tau$ , again comparing readings from STEREO-A (in red) and Parker Solar Probe (in orange). In all panels, circles represent data points corresponding to peak fluxes, while squares specifically indicate those data points where the wavevector azimuth was within  $5^\circ$  of the direct line between STEREO-A and the Sun.

accurate estimation of the decay characteristics of the radio bursts.

We observed that decay times were consistently longer at Parker Solar Probe for frequencies below 1 MHz. However, for data points where  $|\phi_{\text{RTN}}|$  was less than  $5^\circ$ , decay times appeared comparable between both spacecraft, indicating a consistency in certain radio wave propagation characteristics.

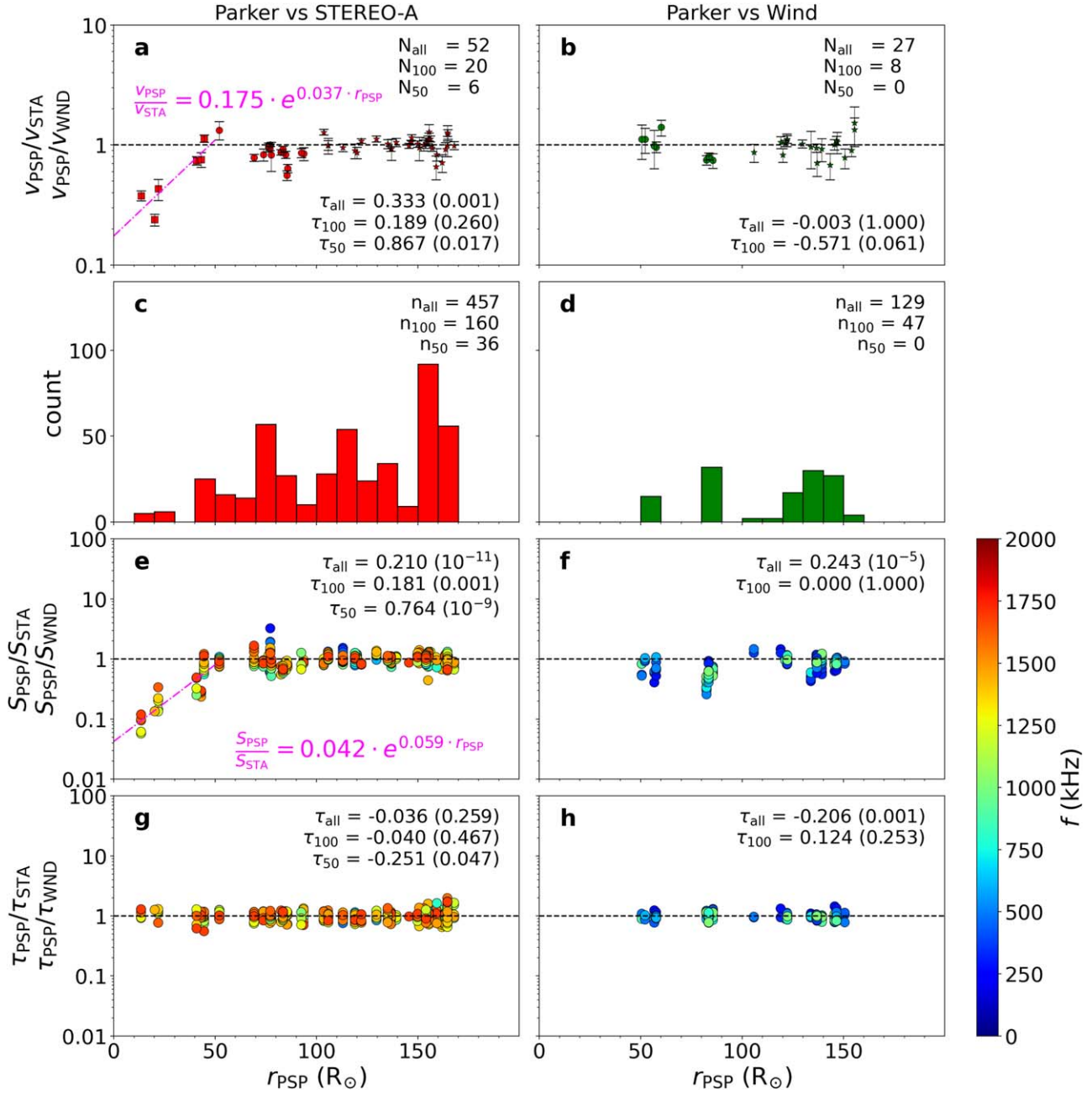
### 2.3. Statistical Analysis

In Figures 4(a) and (b), the ratios of the apparent beam speeds measured by the Parker Solar Probe in comparison to those observed by STEREO-A (for a total of 52 events) and Wind (for a total of 27 events) are demonstrated, following the analytical approach detailed in Section 2.1. Of these, 20 events observed by STEREO-A and 8 by Wind occurred when the Parker Solar Probe was at or beneath a distance of  $100 R_\odot$ . Notably, within a closer proximity of  $50 R_\odot$ , STEREO-A documented six events; in contrast, Wind recorded none at this nearer distance.

To clarify, the apparent discrepancy in the event count, particularly why the sums of events for each threshold do not linearly add up, is due to the nature of our data set organization. Events within the “below  $50 R_\odot$ ” category are also counted within the “below  $100 R_\odot$ ” category, indicating an overlap rather than mutual exclusivity between these subsets.

Moreover, while the majority of the events cataloged occurred in the fall of 2023, a significant portion of the observations capturing the Parker Solar Probe’s proximal approaches to the Sun primarily took place during the spring of 2023 and summer of 2022. This temporal detail is pivotal, underscoring the critical periods within our data set and their respective contributions to our overall analysis.

These ratios, plotted in Figures 4(a) and (b) against the radial distance of the Parker Solar Probe from the Sun, provide insights into the variation of beam speeds with distance. We applied Kendall’s tau coefficient to quantify the correlations in our data set instead of the traditional Pearson correlation as this nonparametric measure is effective in handling outliers and skewed distributions (Kendall 1938). It also enables the direct evaluation of the statistical significance of the correlation’s deviation from zero (Puth et al. 2015). The significance is expressed as a number between 0 and 1, with the value indicating the probability that such a high correlation could have occurred by chance. Statistical significance values for individual Kendall’s tau correlation coefficients are provided in brackets. Our analysis reveals a pronounced trend for STEREO-A data below  $50 R_\odot$ , where electron beam speeds are apparently slower at the Parker Solar Probe compared to STEREO-A, indicated by a Kendall’s tau of 0.867 (0.017). In contrast, the results for Wind are inconclusive due to the absence of data below  $50 R_\odot$ .



In our detailed examination, we directed attention toward six specific events recorded at distances less than  $50 R_\odot$ . These events are represented as circles in Figure 4(a), while the exponential fit that models their behavior is depicted by a magenta dashed-dotted line. This analytical approach led to a significant relationship between the beam speeds measured by the Parker Solar Probe ( $v_{\text{PSP}}$ ) and those by STEREO-A ( $v_{\text{STA}}$ ) as a function of the Parker Solar Probe's radial distance from

the Sun ( $r_{\text{PSP}}$ ). The derived exponential relation is as follows:

$$v_{\text{PSP}}/v_{\text{STA}} = 0.175 \cdot e^{0.037 \cdot r_{\text{PSP}}}. \quad (3)$$

This equation elucidates a clear trend in how relative beam speeds change with the Parker Solar Probe's proximity to the Sun, specifically within the critical zone below  $50 R_\odot$ . The magenta line not only visualizes this trend but also

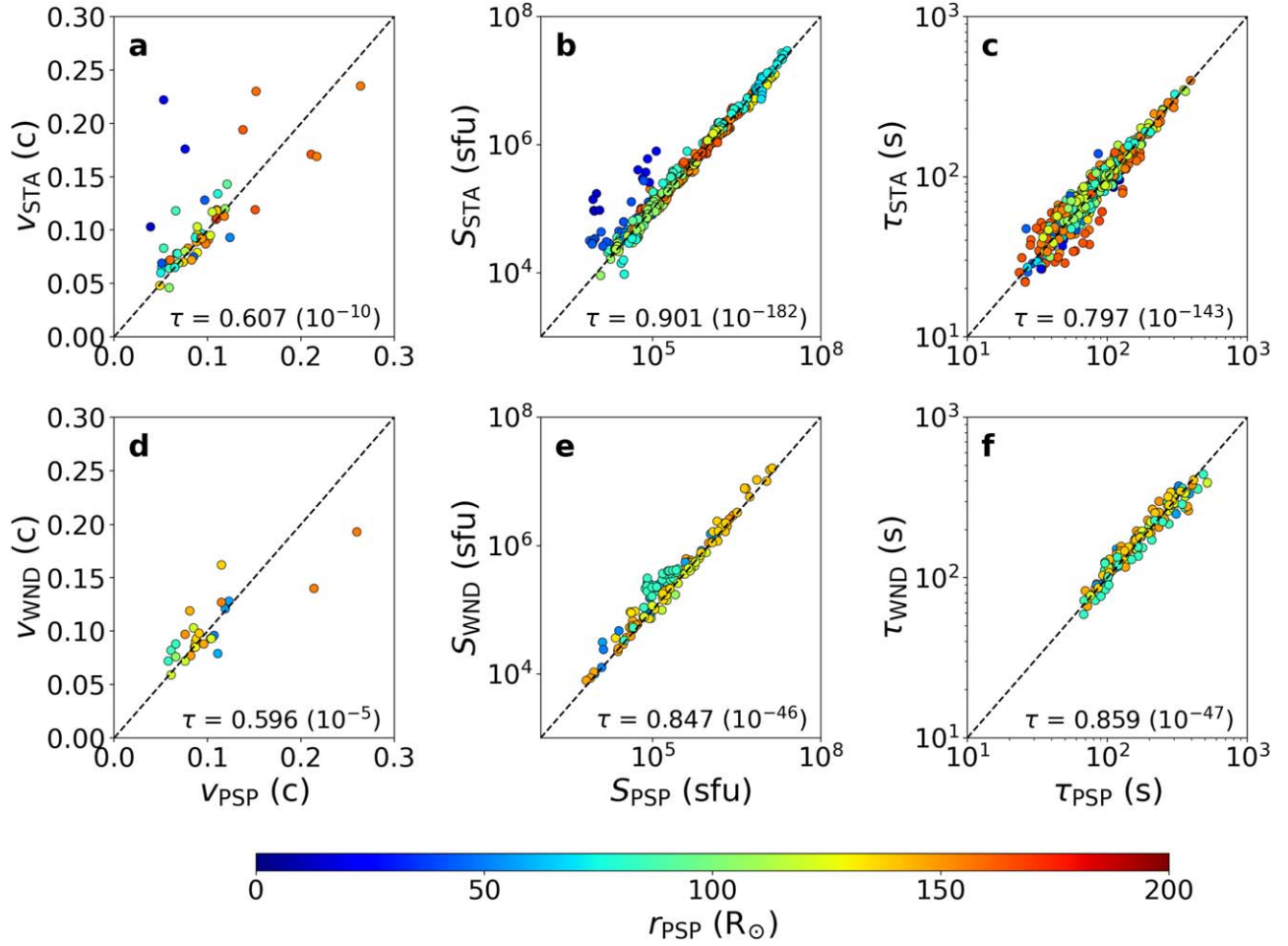


**Figure 5.** Comparative analysis of type III radio burst characteristics as observed by Parker Solar Probe, STEREO-A, and Wind. Panels (a) and (d) compare the beam speeds recorded by STEREO-A and Wind, respectively, with those measured by the Parker Solar Probe, illustrating the relationships and deviations in beam speed across different observational points. Panels (b) and (e) present radio flux measurements, highlighting the comparative intensities of radio emissions as captured by STEREO-A and Wind versus the Parker Solar Probe. Panels (c) and (f) delve into the exponential decay times of the bursts, comparing observations from STEREO-A and Wind against the Parker Solar Probe, respectively. The color gradient across all panels represents the Parker Solar Probe's varying radial distances from the Sun, providing insights into the distance-dependent characteristics of type III radio bursts.

quantitatively supports our observation of systematic variation in beam speed ratios as a function of radial distance.

The analysis then shifts to radio wave propagation, as outlined in Section 2.2. In Figures 4(c) and (d), histograms of frequency bins from type III bursts are presented, with a focus on instances where the wavevector direction was less than  $5^\circ$  from the Sun-spacecraft line for STEREO-A and Wind. We analyzed 457 data points for STEREO-A and 129 for Wind, with 160 and 47 of these points, respectively, occurring when the Parker Solar Probe was below  $100 R_{\odot}$ . For STEREO-A, 36 data points were observed below  $50 R_{\odot}$ , while none were recorded for Wind at this distance. It is important to note that our analysis for Wind was constrained to frequencies below 1040 kHz, as wavevector direction data for this spacecraft were only available in this range, limiting the scope of our investigation with Wind.

In Figures 4(e) and (f), the ratios of radio fluxes recorded by the Parker Solar Probe are compared against those from STEREO-A and Wind. These ratios, plotted against Parker Solar Probe's radial distance from the Sun, show a trend similar to that of the beam speeds. Specifically, radio fluxes at the Parker Solar Probe are systematically lower at distances closer than  $50 R_{\odot}$ , as indicated by a Kendall's tau of  $0.764 (10^{-9})$ .

Adopting the analytical framework used in Figure 4(a), we have calculated an exponential fit for the radio flux ratios ( $S_{\text{PSP}}/S_{\text{STA}}$ ), yielding the following expression:

$$S_{\text{PSP}}/S_{\text{STA}} = 0.042 \cdot e^{0.059 \cdot r_{\text{PSP}}}. \quad (4)$$

Importantly, this exponential relationship is devised to offer a correction specifically for tracking radio sources by multiple spacecraft when the Parker Solar Probe is situated within a range below  $50 R_{\odot}$ , utilizing relative radio flux observations (Krupar et al. 2024b). It addresses the need for a tailored approach to interpret radio flux variations encountered at these closer proximities to the Sun, ensuring more accurate source tracking under these specific conditions.

Figures 4(g) and (h) examine the ratios of exponential decay times  $\tau$  measured by the Parker Solar Probe against those observed by STEREO-A and Wind. Our analysis indicates no significant radial variation in decay times, suggesting consistent propagation characteristics of type III bursts across the data set.

Figure 5 presents alternative visualizations of our data set, offering insights into the behavior of type III radio bursts across different observations. In Figures 5(a) and (d), we compare the beam speeds measured by STEREO-A and Wind to those measured by the Parker Solar Probe. These comparisons reveal



moderate correlations, with Kendall's tau values of 0.638 ( $10^{-11}$ ) for STEREO-A and 0.596 ( $10^{-5}$ ) for Wind, indicating a relationship across the data sets. Notably, at lower radial distances (highlighted in blue), the Parker Solar Probe records lower beam speeds, marking these as outliers. Conversely, events at greater radial distances (marked in red) show varied speeds in both directions, suggesting a broader distribution of observations at these distances.

Figures 5(b) and (e) focus on radio flux measurements from STEREO-A and Wind, respectively, revealing strong correlations (Kendall's tau of 0.901 ( $10^{-182}$ ) for STEREO-A and 0.847 ( $10^{-46}$ ) for Wind). This robust correlation underscores the reliability of our radio flux observations across different spacecraft. We note, however, the presence of clear outliers for low Parker Solar Probe radial distances (in blue) in Figure 5(b). Lastly, Figures 5(c) and (f) explore the decay times for STEREO-A and Wind, respectively. These analyses also indicate strong correlations, with Kendall's tau of 0.797 ( $10^{-143}$ ) for STEREO-A and 0.859 ( $10^{-47}$ ) for Wind, further validating the consistency and reliability of our findings across the various parameters and observation points.

### 3. Discussion and Conclusion

Despite nearly 75 yr of observations, the intricate properties of solar type III radio bursts still elude a comprehensive model. The advent of multispacecraft observations from diverse distances and longitudes has opened new avenues to unravel the complex features of these bursts, particularly in distinguishing their radial and longitudinal properties. Our study focuses on radio emissions observed simultaneously from different solar distances, specifically when the separation angle relative to the Sun was below  $5^\circ$  (Figure 1). We highlight three notable events, with radial separations of 194.1, 186.3, and  $184.6 R_\odot$ , during Parker Solar Probe's encounters 12 and 15 (Section 2.1). In these cases, a plasma line at Parker Solar Probe established a lower-frequency cutoff around 275 kHz. The absence of Langmuir waves in our observations precludes certainty about whether the emissions were fundamental or harmonic.

Utilizing the density model from Kruparova et al. (2023) and the observed frequency drifts, we inferred electron beam speeds under the assumption of fundamental emission and constant radial velocity. Intriguingly, apparent beam speeds at Parker Solar Probe were consistently lower compared to STEREO-A, by factors of 2.6, 4.2, and 2.3 for Cases #1, #2, and #3, respectively. Additionally, we noted a marked discrepancy between the model's predictions at higher frequencies and the actual radio data from the Parker Solar Probe, whereas the model fit the STEREO-A data quite accurately across the full frequency spectrum of the radio bursts. This suggests that while our assumption of constant radial speed aligns well with the observations from STEREO-A, it does not hold as effectively for the Parker Solar Probe.

To clearly demonstrate the notably slower frequency drift at Parker Solar Probe, we examined fixed-frequency light curves for three frequency channels. In Case #1, for instance, the peak times at frequencies of 764 kHz and 367 kHz occur at 00:32 and 00:42, respectively, indicating a drift duration of approximately 10 minutes. In contrast, for similar frequency channels at STEREO-A, the drift takes about 3 minutes, showcasing a much faster rate. This trend of slower drift at Parker Solar Probe compared to STEREO-A is consistently observed in Cases #2 and #3 as well.

A plausible explanation for this discrepancy is the inadequacy of treating radio sources as point sources at these distances. Beaming effects, as these emissions propagate with a significant azimuthal component toward the Parker Solar Probe, might also contribute. While the linear propagation model aligns well with the higher-frequency part of the radio burst at STEREO-A, it does not fit the Parker Solar Probe data, suggesting that the observed beam speeds at Parker Solar Probe are apparently slower. Alternatively, though less likely, the harmonic component could be dominant at Parker Solar Probe, while fundamental emissions prevail at STEREO-A. Given the tendency of the harmonic component to be more diffuse due to a lower refractive index across the inner heliosphere, this could account for the observed variations.

Our statistical analysis of electron beam speeds, based on 52 events with STEREO-A and 27 with Wind (Figures 4(a) and (b)), reveals a strong correlation (Kendall's tau of 0.867 (0.017)) between beam speed ratios and radial distance for STEREO-A. This finding corroborates the theory that the observed discrepancies are predominantly a result of radio source size and beaming effects within  $50 R_\odot$ . Conversely, for Wind, the lack of events below  $50 R_\odot$  precludes conclusive insights. Importantly, no significant correlation is observed for radial distances beyond  $50 R_\odot$ , suggesting that the observed effects are predominantly confined to regions closer to the Sun.

Delving further into radio wave propagation, we utilized direction-finding data from STEREO-A and Wind, positioned near 1 au (Figures 3(a-c)). This enabled us to narrow our data set to radio bursts generated along the Sun-spacecraft line, setting a limit for the absolute value of wavevector azimuth under  $5^\circ$  (Figure 1). Through this lens, we examined individual frequency bins to explore radial variations in radio fluxes and exponential decay times. Mirroring the trend observed in electron beam speeds, we found a notable correlation (Kendall's tau of 0.764) between radio flux ratios and radial distance for events below  $50 R_\odot$  (Figures 4(e) and (f)). This may be caused by propagation of type III bursts into a cone with an opening angle, which decreases with the distance from the Sun up to  $50 R_\odot$ , and stays fixed at larger distances. Above this distance, radio flux ratios displayed no significant variations, suggesting the validity of the point source approximation at greater distances. This result holds implications for the recent radio source localization techniques presented by Krupar et al. (2024b), establishing a lower boundary for employing the von Mises distribution in tracking radio bursts observed by four or more spacecraft.

Lastly, we examined exponential decay times, which provide insights into scattering effects due to density fluctuations in the solar wind (Figures 3(g)-(i)). Our analysis showed generally larger decay times at Parker Solar Probe compared to STEREO-A. This contrasts with findings by Vecchio et al. (2021), who observed larger decay times at Wind, farther from the Sun, than at Solar Orbiter. This discrepancy likely arises from Vecchio et al. (2021) not distinguishing between longitudinal and radial variations. Our focused analysis, excluding data points with wavevector azimuth above  $5^\circ$ , reveals no significant variations in decay times across the cases. Statistical analysis of decay time ratios versus radial distance (Figures 4(g) and (h)) supports the hypothesis that decay times are primarily determined near the radio source, where the wave frequency is not too far from the local electron plasma frequency, with any variations in simultaneous observations attributed to longitudinal effects, as demonstrated by Krupar et al. (2020). This scattering

is hypothesized to be the dominant factor determining the decay times, rather than the radial distance from which the observations are made. As such, whether observed at  $13 R_{\odot}$  or 1 au, the decay times remain comparable when stemming from the same radio source.

This study marks a significant advancement in understanding the elusive nature of solar type III radio bursts, leveraging multispacecraft observations to unravel their complex radial and longitudinal properties. Our detailed examination of emissions observed simultaneously from varying solar distances underlines the influence of radio source size and beaming effects, particularly within  $50 R_{\odot}$ . The observed lower beam speeds at the Parker Solar Probe, as compared to STEREO-A, challenge the conventional point source approximation and hint at intricate propagation dynamics involving azimuthal components. Furthermore, the absence of a similar trend beyond  $50 R_{\odot}$  and the lack of conclusive insights from Wind data due to limited observations emphasize the complexity of these phenomena.

The study also sheds light on the radio wave propagation characteristics, as revealed by the correlation between radio flux ratios and radial distances for events below  $50 R_{\odot}$ . This finding not only corroborates the beam speed trends but also suggests the validity of point source approximation for greater distances, influencing radio source localization techniques. Additionally, our analysis of exponential decay times, contrary to previous studies, indicates that these times are largely uniform across different cases when longitudinal effects are isolated. This uniformity implies that the observed decay times are primarily shaped near the radio source, influenced by scattering effects in the solar wind.

Collectively, these insights contribute to a more nuanced understanding of type III radio bursts, underlining the need for considering both radial and longitudinal variations in their analysis.

This study paves the way for future explorations into the intricate mechanisms governing solar radio emissions, potentially refining models and techniques in solar physics research.

### Acknowledgments

Parker Solar Probe was designed, built, and is now operated by the Johns Hopkins Applied Physics Laboratory as part of NASA's Living with a Star (LWS) program (contract NNN06AA01C). Support from the LWS management and technical team has played a critical role in the success of the Parker Solar Probe mission. The FIELDS instrument suite was designed and built and is operated by a consortium of institutions including the University of California, Berkeley, University of Minnesota, University of Colorado, Boulder, NASA/GSFC, CNRS/LPC2E, University of New Hampshire, University of Maryland, UCLA, IFRU, Observatoire de Meudon, Imperial College, London, and Queen Mary University of London. Solar Orbiter is a space mission of international collaboration between ESA and NASA, operated by ESA. The authors would like to thank the many individuals and institutions who contributed to making STEREO and Wind possible. V.K. was supported by the STEREO/WAVES and Wind/WAVES projects, and by the NASA grant 19-HSR-19\_2-0143. We utilized Wind/WAVES/RAD1 Level 3 data available from [https://maser.obspm.fr/repository/wind/waves/wi\\_wa\\_rad1\\_l3\\_df\\_v02/data/](https://maser.obspm.fr/repository/wind/waves/wi_wa_rad1_l3_df_v02/data/). Additional radio data employed in this study can be accessed through the public repository at <https://spdf.gsfc.nasa.gov/>.

### Appendix Spacecraft Orbits

Our analysis commenced with the identification of time intervals where the Parker Solar Probe was nearly radially aligned with either STEREO-A or Wind, up to 2023 December.

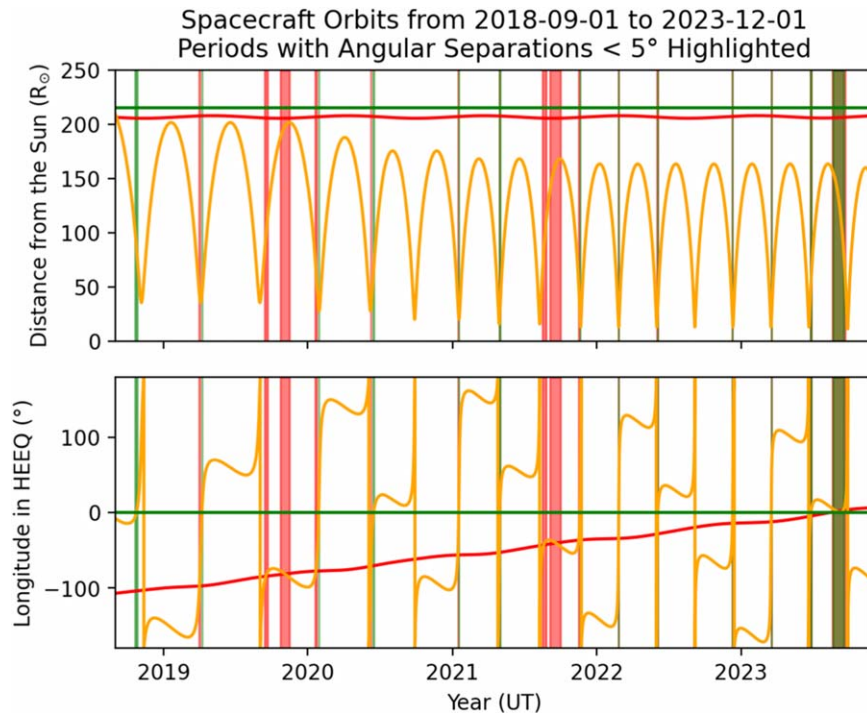


**Figure 6.** Spacecraft orbits from 2018 September 1 to 2023 December 1. The top panel shows the radial distances of Parker Solar Probe (orange), STEREO-A (red), and Wind (green) from the Sun. The bottom panel details their longitudinal positions relative to the Sun, with the same color scheme for consistency. Periods of significant radial alignment, where Parker Solar Probe and STEREO-A or Wind are within  $5^\circ$  of each other longitudinally, are marked by red (or green) rectangles, highlighting these key alignment periods for analysis.

**Table 1**  
Intervals of Radial Alignment for Parker Solar Probe with STEREO-A and Wind (Separation Angle  $<5^\circ$ )



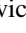
Spacecraft	Start Time (UT)	End Time (UT)	$\Delta R_{\max}$ ( $R_\odot$ )	Number of Bursts
Wind	2018-10-21 12:14	2018-10-26 07:27	136.5	0
STEREO-A	2019-04-01 09:42	2019-04-02 05:11	166.6	0
Wind	2019-04-07 13:30	2019-04-08 08:26	174.4	0
STEREO-A	2019-09-14 01:02	2019-09-21 01:13	120.5	0
STEREO-A	2019-10-22 12:51	2019-11-14 14:49	18.9	0
STEREO-A	2020-01-19 17:20	2020-01-22 09:36	146.4	0
Wind	2020-01-28 04:58	2020-01-28 14:48	186.3	0
STEREO-A	2020-06-08 08:54	2020-06-08 19:14	178.0	0
Wind	2020-06-14 03:16	2020-06-16 14:14	155.8	0
STEREO-A	2021-01-14 07:27	2021-01-15 01:25	173.5	0
Wind	2021-01-16 21:43	2021-01-17 03:53	193.8	0
STEREO-A	2021-04-29 15:48	2021-04-29 19:48	191.2	0
Wind	2021-04-30 19:53	2021-05-01 05:07	191.6	0
<b>STEREO-A</b>	<b>2021-08-17 07:14</b>	<b>2021-08-26 07:46</b>	<b>138.0</b>	<b>2</b>
<b>STEREO-A</b>	<b>2021-09-05 11:21</b>	<b>2021-09-30 17:07</b>	<b>64.5</b>	<b>12</b>
STEREO-A	2021-11-15 04:32	2021-11-17 08:56	161.5	0
Wind	2021-11-19 13:35	2021-11-19 22:55	192.8	0
STEREO-A	2022-02-25 07:26	2022-02-25 10:26	194.2	0
Wind	2022-02-25 17:17	2022-02-25 20:05	201.7	0
<b>STEREO-A</b>	<b>2022-06-03 01:37</b>	<b>2022-06-03 08:41</b>	<b>186.8</b>	<b>2</b>
Wind	2022-06-04 04:52	2022-06-04 23:39	184.9	0
STEREO-A	2022-12-10 00:18	2022-12-10 08:08	186.6	0
Wind	2022-12-10 10:48	2022-12-10 16:18	197.4	0
<b>STEREO-A</b>	<b>2023-03-18 00:25</b>	<b>2023-03-18 03:20</b>	<b>194.2</b>	<b>1</b>
Wind	2023-03-18 04:01	2023-03-18 07:12	201.1	0
<b>STEREO-A</b>	<b>2023-06-25 15:31</b>	<b>2023-06-27 08:12</b>	<b>165.0</b>	<b>4</b>
<b>Wind</b>	<b>2023-06-26 07:21</b>	<b>2023-06-28 14:40</b>	<b>168.9</b>	<b>5</b>
<b>STEREO-A</b>	<b>2023-08-19 21:00</b>	<b>2023-09-20 20:13</b>	<b>138.4</b>	<b>31</b>
<b>Wind</b>	<b>2023-08-21 20:04</b>	<b>2023-09-18 19:18</b>	<b>135.3</b>	<b>22</b>

**Note.** Table 1 enumerates the time intervals of such radial alignments, including the maximal radial separation and the number of type III bursts observed during each period, highlighted in bold.

Figure 6 showcases the orbits of these spacecraft in the HEEQ coordinate system. This depiction is essential for understanding their relative positions and movements in relation to the Sun. The primary selection criterion for our analysis was the radial alignment of the Parker Solar Probe with STEREO-A or Wind. We specifically focused on intervals where the Parker Solar Probe was within  $5^\circ$  of radial alignment with either spacecraft. This criterion was vital to isolate type III radio bursts observable simultaneously by multiple spacecraft, allowing a more holistic analysis of their properties. Table 1 enumerates the time intervals of such radial alignments, including the maximal radial separation and the number of type III bursts observed during each period. Notably, a surge in solar activity in 2023 corresponded with an increase in the number of observed events. This table also serves as an essential reference for researchers focusing on radial alignments with the Parker Solar Probe, aiding in the identification of significant observational periods.

### ORCID iDs

Vratislav Krupar  <https://orcid.org/0000-0001-6185-3945>  
 Oksana Kruparova  <https://orcid.org/0000-0002-1122-6422>  
 Adam Szabo  <https://orcid.org/0000-0003-3255-9071>  
 Lynn B. Wilson, III  <https://orcid.org/0000-0002-4313-1970>  
 Frantisek Nemec  <https://orcid.org/0000-0002-3233-2718>  
 Ondrej Santolik  <https://orcid.org/0000-0002-4891-9273>  
 Marc Pulupa  <https://orcid.org/0000-0002-1573-7457>

Karine Issautier  <https://orcid.org/0000-0002-2757-101X>  
 Stuart D. Bale  <https://orcid.org/0000-0002-1989-3596>  
 Milan Maksimovic  <https://orcid.org/0000-0001-6172-5062>

### References

- Badman, S. T., Carley, E., Cañizares, L. A., et al. 2022, *ApJ*, **938**, 95  
 Bale, S. D., Goetz, K., Harvey, P. R., et al. 2016, *SSRv*, **204**, 49  
 Bastian, T. S. 1994, *ApJ*, **426**, 774  
 Bonnin, X., Hoang, S., Cecconi, B., & Issautier, K. 2023, Wind/Waves/RAD1  
 LESIA L3 DF Data Collection, v02, PADC, doi:10.25935/hegh-1r24  
 Bonnin, X., Hoang, S., & Maksimovic, M. 2008, *A&A*, **489**, 419  
 Bougeret, J. L., Goetz, K., Kaiser, M. L., et al. 2008, *SSRv*, **136**, 487  
 Bougeret, J. L., Kaiser, M. L., Kellogg, P. J., et al. 1995, *SSRv*, **71**, 231  
 Cairns, I. H., & Robinson, P. A. 1995, *GeoRL*, **22**, 3437  
 Cecconi, B., Bonnin, X., Hoang, S., et al. 2008, *SSRv*, **136**, 549  
 Chen, X., Kontar, E. P., Chrysaphi, N., et al. 2023, *A&A*, **680**, A1  
 Dulk, G. A. 2000, *GMS*, **119**, 115  
 Dulk, G. A., & Suzuki, S. 1980, *A&A*, **88**, 203  
 Fox, N. J., Velli, M. C., Bale, S. D., et al. 2016, *SSRv*, **204**, 7  
 Ginzburg, V. L., & Zhelezniakov, V. V. 1958, *SvA*, **2**, 653  
 Gopalswamy, N., Aguilar-Rodriguez, E., Yashiro, S., et al. 2005, *JGRA*, **110**, A12S07  
 Hoang, S., Steinberg, J. L., Stone, R. G., Zwickl, R. H., & Fainberg, J. 1981, *JGR*, **86**, 4531  
 Kaiser, M. L., Kucera, T. A., Davila, J. M., et al. 2008, *SSRv*, **136**, 5  
 Kellogg, P. J. 1980, *ApJ*, **236**, 696  
 Kendall, M. G. 1938, *Biometrika*, **30**, 81  
 Kontar, E. P., Chen, X., Chrysaphi, N., et al. 2019, *ApJ*, **884**, 122  
 Kontar, E. P., Emslie, A. G., Clarkson, D. L., et al. 2023, *ApJ*, **956**, 112  
 Kontar, E. P., Yu, S., Kuznetsov, A. A., et al. 2017, *NatCo*, **8**, 1515  
 Krupar, V., Kruparova, O., Szabo, A., et al. 2024a, *ApJ*, **960**, 101



- Krupar, V., Kruparova, O., Szabo, A., et al. 2024b, [ApJ](#), **961**, 88
- Krupar, V., Maksimovic, M., Kontar, E. P., et al. 2018, [ApJ](#), **857**, 82
- Krupar, V., Maksimovic, M., Santolik, O., Cecconi, B., & Kruparova, O. 2014, [SoPh](#), **289**, 4633
- Krupar, V., Nguyen, Q., Bonnin, X., Cecconi, B., & Maksimovic, M. 2022, STEREO/Waves/LFR-HFR L3 DF Data Collection, v1.0, PADC/MASER, doi:[10.25935/4TAK-5225](#)
- Krupar, V., Santolik, O., Cecconi, B., et al. 2012, [JGRA](#), **117**, A06101
- Krupar, V., Szabo, A., Maksimovic, M., et al. 2020, [ApJS](#), **246**, 57
- Kruparova, O., Krupar, V., Szabo, A., Pulupa, M., & Bale, S. D. 2023, [ApJ](#), **957**, 13
- Leblanc, Y., Dulk, G. A., & Bougeret, J.-L. 1998, [SoPh](#), **183**, 165
- Manning, R., & Fainberg, J. 1980, *SSI*, **5**, 161
- Musset, S., Maksimovic, M., Kontar, E., et al. 2021, [A&A](#), **656**, A34
- Pulupa, M., Bale, S. D., Bonnell, J. W., et al. 2017, [JGRA](#), **122**, 2836
- Puth, M.-T., Neuhäuser, M., & Ruxton, G. D. 2015, [Anim. Behav.](#), **102**, 77
- Reid, H. A. S., & Ratcliffe, H. 2014, [RAA](#), **14**, 773
- Reiner, M. J., Fainberg, J., Kaiser, M. L., & Stone, R. G. 1998, [JGR](#), **103**, 1923
- Sharykin, I. N., Kontar, E. P., & Kuznetsov, A. A. 2018, [SoPh](#), **293**, 115
- Steinberg, J. L., Hoang, S., Lecacheux, A., Aubier, M. G., & Dulk, G. A. 1984, [A&A](#), **140**, 39
- Tapping, K. F. 2013, [SpWea](#), **11**, 394
- Vecchio, A., Maksimovic, M., Krupar, V., et al. 2021, [A&A](#), **656**, A33
- Wild, J. P. 1950, [AuSRA](#), **3**, 541
- Wilson, L. B., III, Brosius, A. L., Gopalswamy, N., et al. 2021, [RvGeo](#), **59**, e2020RG000714